Supplementary Material for

Dynamically controlling terahertz wave-fronts with cascaded metasurfaces

Xiaodong Cai[a,†], Rong Tang[a,†], Haoyang Zhou[b,†],Qiushi Li[a], Shaojie Ma[b,c], Dongyi Wang[b], Tong Liu[b], Xiaohui Ling[b,g], Wei Tan[e,f], Qiong He[b,c,d], Shiyi Xiao[a,*], and Lei Zhou[b,d,*]

[a]Shanghai University, Key Laboratory of Specialty Fiber Optics and Optical Access Networks, Joint International Research Laboratory of Specialty Fiber Optics and Advanced Communication, Shanghai Institute for Advanced Communication and Data Science, Shanghai, China, 200444

[b]Fudan University, State Key Laboratory of Surface Physics, Key Laboratory of Micro and Nano Photonic Structures (Ministry of Education) and Physics Department, Shanghai, China, 200433

[c]Fudan University, Academy for Engineering and Technology, Shanghai, China, 200433

[d]Collaborative Innovation Centre of Advanced Microstructures, Nanjing, China, 210093

[e]CAEP, Microsystem and Terahertz Research Center, Chengdu, Sichuan, China, 610200

[f]CAEP, Institute of Electronic Engineering, Mianyang, Sichuan, China, 621999

[g]Hengyang Normal University, College of Physics and Electronic Engineering, Hengyang, China, 421002

*Corresponding Authors: phxiao@shu.edu.cn, phzhou@fudan.edu.cn
†These authors contributed equally to this work.

List of contents

I. Derivation of Equation (2)

The transmission Jones matrix for the system with a rotated local axis in the circular-polarization (CP) representation is given by:

$$\tilde{\mathbf{T}}_i(\mathbf{r},t) = \mathbf{R}^{-1}\mathbf{S}_i^{-1}(t)\begin{pmatrix} e^{i\Phi_u^i(\mathbf{S}_i(t)\cdot\mathbf{r})} & 0 \\ 0 & e^{i\Phi_v^i(\mathbf{S}_i(t)\cdot\mathbf{r})} \end{pmatrix}\mathbf{S}_i(t)\mathbf{R}, \tag{S1}$$

where $\mathbf{S}_i(t)$ and $\mathbf{R}$ are defined in Eq. (1) in the main text.

Utilizing the Pauli matrixes, we get:

$$\begin{aligned}\tilde{\mathbf{T}}_i(\mathbf{r},t) &= \frac{e^{i\Phi_u^i(\mathbf{S}_i(t)\cdot\mathbf{r})} + e^{i\Phi_v^i(\mathbf{S}_i(t)\cdot\mathbf{r})}}{2}\hat{\mathbf{I}} - \frac{e^{i\Phi_v^i(\mathbf{S}_i(t)\cdot\mathbf{r})} - e^{i\Phi_u^i(\mathbf{S}_i(t)\cdot\mathbf{r})}}{2} \\ &\quad \cdot\left[\cos[2\alpha_i(t)]\sigma_x + \sin[2\alpha_i(t)]\sigma_y + 0\sigma_z\right] \\ &= \exp\left[-i\Delta\Phi^i(\mathbf{r},t)\cdot\hat{n}_i(t)\cdot\vec{\sigma}/2\right]\exp\left[i\Phi_{\mathbf{av}}^i(\mathbf{r},t)\right]\end{aligned} \tag{S2}$$

which is as Eq. (2) in the main text. With regards to that case, Ref. 45 has rigorously demonstrated that the first term, $\exp\left[-i\Delta\Phi^i(\mathbf{r},t)\cdot\hat{n}_i(t)\cdot\vec{\sigma}/2\right]$, can be described as a rotation by an angle of $\Delta\Phi^i(\mathbf{r},t) = \Phi_v^i(\mathbf{S}_i(t)\cdot\mathbf{r}) - \Phi_u^i(\mathbf{S}_i(t)\cdot\mathbf{r})$, with respect to a certain axis, $\hat{n}_i(t) = \cos[2\alpha_i(t)]\hat{x} + \sin[2\alpha_i(t)]\hat{y}$, on the Poincaré's sphere.

II. $\{\theta,\varphi\} \sim \{\alpha_1(t),\alpha_2(t)\}$ relationship for designed meta-devices

With the total phase of the designed meta-device $\Phi_{\mathbf{av}}(\mathbf{r},t) = \xi_0\left[x(\cos\alpha_1(t) + \cos\alpha_2(t)) + y(\sin\alpha_1(t) + \sin\alpha_2(t))\right]$ at hand (see Eq. (8) in the main text), we can derive the total phase gradient:

$$\begin{aligned}\xi_{\mathbf{tot}} &= \nabla\Phi_{\mathbf{av}}(\mathbf{r},t) \\ &= 2\xi_0\cos\left(\frac{\alpha_1(t) - \alpha_2(t)}{2}\right)\left[\hat{x}\cos\left(\frac{\alpha_1(t) + \alpha_2(t)}{2}\right) + \hat{y}\sin\left((\frac{\alpha_1(t) + \alpha_2(t)}{2})\right)\right],\end{aligned} \tag{S3}$$

with the magnitude as:

$$\left|\xi_{\mathbf{tot}}\right| = 2\xi_0\cos\left(\frac{\alpha_1(t) - \alpha_2(t)}{2}\right). \tag{S4}$$

We then obtain the re-directing polar angle θ and azimuth angle φ for a normally

incident wave with $\theta_i = 0$, which according to the generalized Snell's law, is as:

$$\begin{cases} \theta = \sin^{-1}\left[2\xi_0 / k_0 \cos\left[(\alpha_1(t) - \alpha_2(t))/2\right]\right] \\ \varphi = [\alpha_1(t) + \alpha_2(t)]/2 \end{cases},$$ (S5)

with the corresponding phase diagrams shown in Figs. 4a and b in the main text.

III. Fabrication of samples

All dielectric samples were fabricated as per the following:

(1) Thinning and polishing: Thin and polish the high-resistance 1mm thick film to 545 μm.

(2) Cleaning: Acetone ultrasonic cleaning is carried out for 10 minutes, followed by isopropanol ultrasonic cleaning for 10 minutes, deionized water ultrasonic cleaning for 10 minutes, rinsing with deionized water three times, and then ultrasonic cleaning with a mixed solution of ammonia, hydrogen peroxide and water for 10 minutes. Finally, dry with a nitrogen gun.

(3) Front lithography: a) Gumming: AZ4620, 1000r/min, 30s; b) pre-baking: 100°C, 10min, gum thickness 8um; c) exposure: MA6; d) development: 20% TMAH and deionized water at a ratio of 1:7, mixed and developed for 3 minutes; e) microscopic examination; f) film: 110°C, 10min.

(4) Etching: HSE deep silicon etching machine etching, with a target etching depth of 240um.

(5) Gum and clean, followed by ultrasonic cleaning with acetone for 10 minutes, ultrasonic cleaning with isopropanol for 10 minutes, ultrasonic cleaning with deionized water for 10 minutes, rinsing with deionized water three times, and ultrasonic cleaning with a mixed solution of ammonia, hydrogen peroxide and water for 10 minutes. Dry with a nitrogen gun.

(6) M4L plasma remover is used to treat the back side, oxygen 300W, 5min.

(7) Back lithography: a) Gum: AZ4620, 1000r/min, 30s; b) pre-baking: 100°C, 10min, gum thickness 8um; c) exposure: MA6, and the back is aligned and engraved; d) development: 20% TMAH and deionized water at a ratio of 1:7, mixed and

developed for 3 minutes; e) microscopic examination; f) film: 110°C, 10min.

(8) Etching: HSE deep silicon etching machine etching, and the target etching depth is 195um.

(9) Laser scribing.

(10) Degumming and cleaning, followed by ultrasonic cleaning with acetone for 10 minutes, ultrasonic cleaning with isopropanol for 10 minutes, ultrasonic cleaning with deionized water for 10 minutes, rinsing with deionized water three times, and ultrasonic cleaning with a mixed solution of ammonia, hydrogen peroxide and water for 10 minutes.

(11) Taking the film: Put the film on a hot plate at 150C° and bake for 30-60s, whereby the film will lose its viscosity and warp. Use tweezers to then gently remove the film from the substrate.
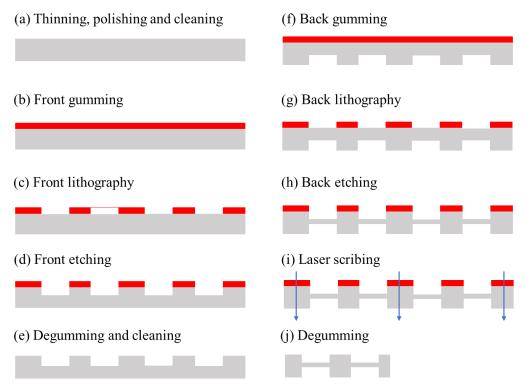
(a) Thinning, polishing and cleaning

(b) Front gumming

(c) Front lithography

(d) Front etching

(e) Degumming and cleaning

(f) Back gumming

(g) Back lithography

(h) Back etching

(i) Laser scribing

(j) Degumming

Figure S1. (a-j) Process of sample fabrication.

3

IV. Design and optimization of two meta-devices

Supplementary Table 1. Top- and bottom-view of the meta-atoms and their physical dimensions for the dynamic beam-steering meta-device.

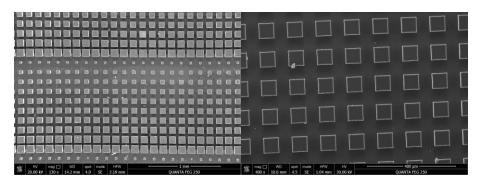| meta-atom (top and bottom)	h_1 (µm)	l (µm)	h_3 (µm)	w_x (µm)	w_y (µm)	Φ_u (°)	Φ_v (°)
	240	32	50	72	72	0	0
	240	49.8	50	72	72	29.7	29.6
	240	60	50	72	72	64.3	64.4
	240	68	50	72	72	102.4	102.4
	240	73.8	50	72	72	136.6	136.6
	240	78.5	50	72	72	167.3	167.4
	240	83	50	72	72	198.3	198.5
	240	89.2	50	72	72	238.6	238.6
	240	97.8	50	72	72	285.7	285.7
	240	105	50	72	72	322.8	322.8

Figure S2. Scanning Electronic Microscope (SEM) images of dynamic beam-steering meta-device: (left) top-view and (right) bottom-view.

Supplementary Table 2. Top- and bottom-view of the meta-atoms and their physical dimensions for the meta-device on dynamic beam-steering and polarization control capabilities.
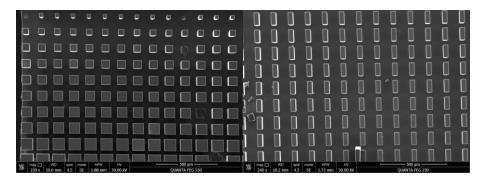
meta-atom (top and bottom)	h_1 (μm)	L (μm)	h_3 (μm)	w_x (μm)	w_y (μm)	Φ_u (°)	Φ_v (°)
	240	32	230	94	40	90	0
	240	52.6	230	94	40	128.1	35.6
	240	62.7	230	94	40	165.8	72.3
	240	69.3	230	94	40	200.5	107.4
	240	74.8	230	94	40	235.2	140.5
	240	81.7	230	94	40	277.6	179.6
	240	88.4	230	94	40	313.8	216.2
	240	94	230	94	40	345.5	251.7
	240	100.3	230	94	40	384.9	294.3
	240	105.4	230	94	40	415.1	323.3

Figure S3. Scanning Electronic Microscope (SEM) images of the dynamic beam and polarization control meta-device: (left) top-view and (right) bottom-view.
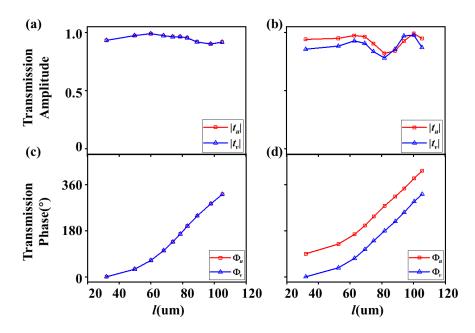
Figure S4. Simulated spectra of the transmission amplitudes (a,b) and phase (c,d) along two orthogonal directions of meta-atoms illuminated by normal incident $\hat{u}$- and $\hat{v}$-polarized beams for the meta-device for dynamic beam-steering and polarization control capabilities.

V. Experimental setup

The performance of our designed cascaded metasurface was measured using a terahertz time-domain spectroscopy (THz-TDS) system. As shown in Fig. S5, the linear polarized terahertz wave emitted from the transmitter was first collected by a dielectric lens and converted to circular polarization when passing through the quarter-wave plate (QWP), and then, using the same lens, the terahertz (THz) light was refocused to the receiver after passing through the samples. The cascaded samples (that with pre-designed angular speeds controlled by a rotating stage are able to rotate mechanically, see Fig. S6) were placed in the center of a rotating stage with the phase gradient going along in the horizontal direction, and finally the linearly polarized receiver was also fixed on another rotation stage in order to collect the THz wave for two linear polarizations. By rotating the rotation stage from –90° to +90°, the diffraction wave was detected every 2°. The cascaded metasurfaces were driven by two electric-controlled rotators so as to individually control the rotating speed of each metasurface, where the rotation speed can be adjusted from 0-360 degrees/second. At the same time, each rotator can be programed to rotate to a fixed angle with an angle resolution at 0.05
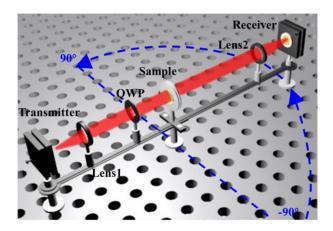
degrees.

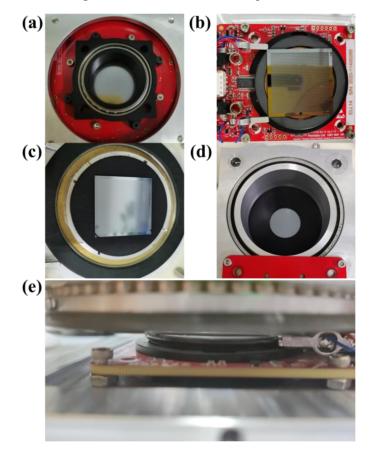**Figure S5.** Far-field measurement platform.

Figure S6. Photograph of the bottom view (a,c) and top view (b,d) of layers 1 and 2 when the two layers are loaded on the motorized rotation stage; and the side view of the motorized rotation stage (e).

VI. Optimization of the spacing distance between layers

As shown in Figs. S7-S10, we found that the efficiency of wave manipulation

decayed as the spacing distance increased, while the spacing distance of 200 μm has the highest wave manipulation efficiency. However, realizing such a close distance (200 μm) during an experiment is very difficult. Therefore, in order to compromise the optimization of the device's performance for the practical realization of the experiments, the spacing distance was finally fixed to 600 μm.
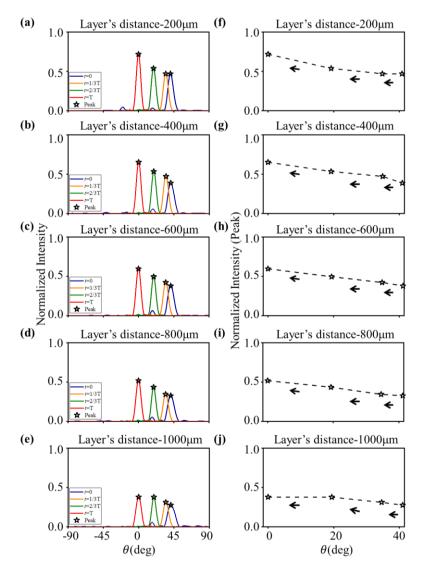

Figure S7. The far-field scattering power distribution for the isotropic metasurface, at four different time instants, when varying the spacing distance between layers from 200 μm to 1000 μm, with the isotropic metasurface evolving with $\{\omega_1 = -\pi/(2T), \omega_2 = \pi/(2T)\}$ (a-e). The corresponding peak values of the far-field scattering power distribution (f-j).
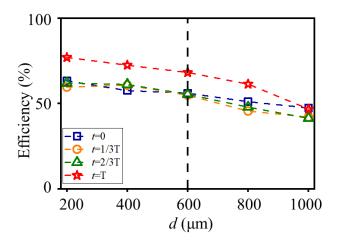
Figure S8. The total efficiency of the isotropic metasurface when varying the spacing distance between layers from 200 μm to 1000 μm, with the isotropic metasurface evolving with $\{\omega_1 = -\pi/(2T), \omega_2 = \pi/(2T)\}$.
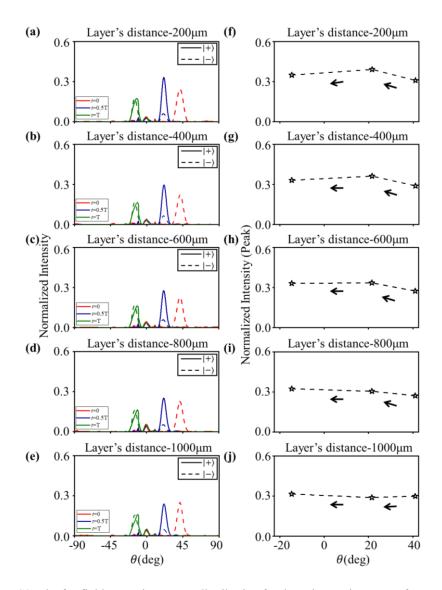

Figure S9. The far-field scattering power distribution for the anisotropic metasurface at three

9

different time instants, when varying the spacing distance between layers from 200 μm to

1000 μm, with the anisotropic metasurface evolving with $\{\omega_1 = -\pi/(2T), \omega_2 = 3\pi/(4T)\}$

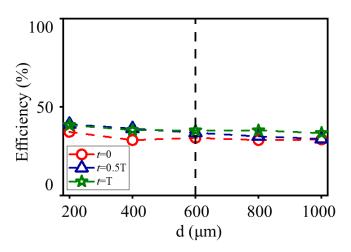(a-e). The corresponding peak values of the far-field scattering power distribution (f-j).

Figure S10. The total efficiency for the anisotropic metasurface when varying the spacing

distance between layers from 200 μm to 1000 μm, with the anisotropic metasurface evolving

with $\{\omega_1 = -\pi/(2T), \omega_2 = 3\pi/(4T)\}$.

VII. The relationship between the size of samples and the spacing distance

Figure S11 plots out how light beams illuminate on the meta-device. The incident

wave (with a beam width of 5 mm) illuminates the area (denoted as the red-dashed

circle with a diameter D_1) on the first metasurface (Layer 1). After passing through

this layer of the metasurface, the deflected wave will then illuminate the area with the

same diameter but with a shifted center as $H \tan\theta_1$ (H denotes the spacing distance

between two layers). When the beam is dynamically steered, both metasurface layers

must be rotated, thereupon the illuminated area is also rotated and will cover the blue-

dashed circle area (with the diameter D_2) on the second metasurface (Layer 2). As

shown in Fig. S11b, the relationship between the diameters of the two illuminating areas

is calculated as $H \tan\theta_1 \leq (D_2 - D_1)/2$ with $\theta_1 = \arcsin(\xi_0/k_0)$ (the illuminating

area on Layer 2 is larger than that on Layer 1). During the design process of our

10

experiments, we carefully considered this issue, where the size of Layer 2 is much larger than the illuminating region, with $D_2 \geq 2H\tan\theta_1 + D_1$ (Region I in Fig. S11c).
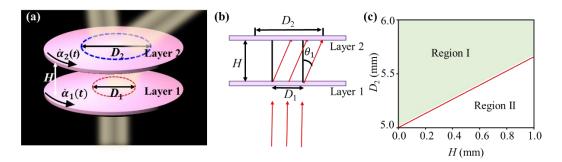

Figure S11. Schematic of cascaded metasurfaces, light beams and illuminating area (a, b). The optimized region for the diameter of Layer 2 as a function of the spacing distance H (c).

VIII. Calculations of the deflection efficiencies for meta-devices

Here, we present the quantitative calculations of the deflection efficiencies of fabricated meta-devices. In order to obtain quantitative estimations on the deflection efficiencies, we integral the widths of the deflected beams to get the total deflection powers. For the reference signal, we integral the total power over the entire beam width of the transmitted beam in the air. The deflection efficiency can then be calculated as:

$$\eta_\lambda = \frac{\int_{\text{Meta}}\left|\left(\mathbf{E}^\lambda\right)^* \cdot \mathbf{E}_\mathbf{k}^{sca}\right|^2 d\Omega_\mathbf{k}}{\int_{\text{Air}}\left|\left(\mathbf{E}^+\right)^* \cdot \mathbf{E}_\mathbf{k}^{in}\right|^2 d\Omega_\mathbf{k}} \quad \text{and} \quad \eta_{-\lambda} = \frac{\int_{\text{Meta}}\left|\left(\mathbf{E}^{-\lambda}\right)^* \cdot \mathbf{E}_\mathbf{k}^{sca}\right|^2 d\Omega_\mathbf{k}}{\int_{\text{Air}}\left|\left(\mathbf{E}^+\right)^* \cdot \mathbf{E}_\mathbf{k}^{in}\right|^2 d\Omega_\mathbf{k}}, \tag{S6}$$

where $\mathbf{E}^\lambda$ and $\mathbf{E}^{-\lambda}$ represent the theoretically predicted polarization of the transmitted wave and its orthogonal polarization state (calculated by Eq. 11 in the main text); $\mathbf{E}^+$ and $\mathbf{E}^-$ represent the polarization states of the left circular polarization (LCP) wave and right circular polarization (RCP) wave; and $\mathbf{E}_\mathbf{k}^{sca}$ and $\mathbf{E}_\mathbf{k}^{in}$ denote the measured (or simulated) electric field and the incident electric field for different scattering directions (denoted by $\mathbf{k}$).

Figures S12 and S13 demonstrate the experimentally measured and simulated spectra and deflection efficiency of the dynamic beam-steering meta-device that

evolves along Path I and Path II under normal LCP incidence. Here, the red curves and blue curves denote the experimental and simulated spectra of LCP (the theoretical predicted polarization state) and the spectra of RCP (the orthogonal polarization to the predicted one). We note that both the experimental and simulated deflection efficiency is around the 50% mark.
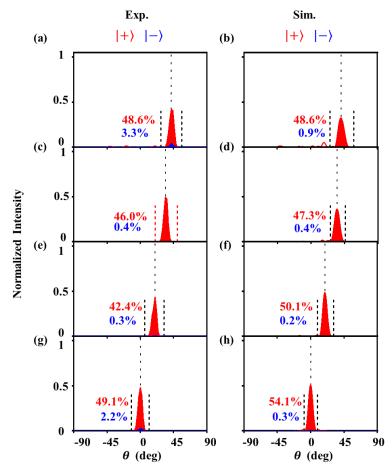

Figure S12. Measured normalized angular power distributions of the scattered field of transmitted $|+\rangle$ (LCP) component and $|-\rangle$ (RCP) component, when the dynamic beam-steering meta-device is evolving along Path I for a normal LCP incidence (a, c, e, g). The corresponding simulation results are represented in b, d, f, h. The retrieved values of the efficiency of deflection are indicated in a-h.
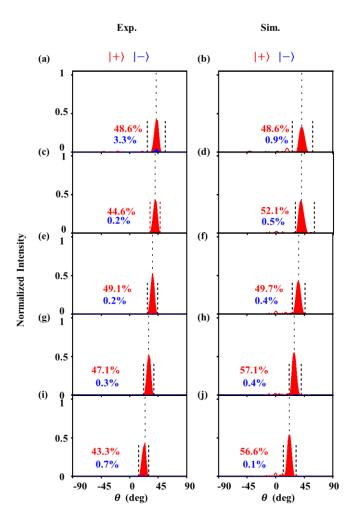
Figure S13. Measured normalized angular power distributions of the scattered field of transmitted $|+\rangle$ component and $|-\rangle$ component when the dynamic beam-steering meta-device evolves along Path II for a normal LCP incidence (a, c, e, g, i). The corresponding simulation results are represented in b, d, f, h, j. The retrieved values of the deflection efficiencies are indicated in a-j.

Figure S14 demonstrates the experimentally measured and simulated spectra and deflection efficiency of the meta-device for dynamic beam-steering and polarization manipulation. Here, we rotate two layered metasurfaces with the speeds of $\{\omega_1 = -\pi/(2T), \omega_2 = 3\pi/(4T)\}$ at a certain three times. The red and blue curves denote the experimental and simulated spectra of the polarization states predicted by theory and its orthogonal polarization states at certain time instants. We note that both the experimental and simulated deflection efficiency is around the 35% mark.
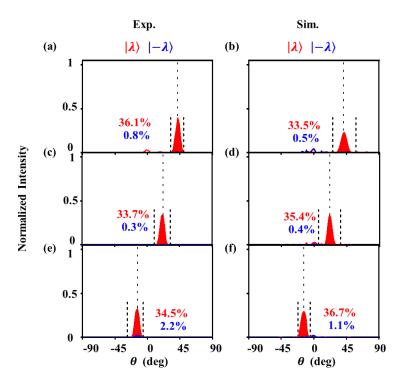
Figure S14. Measured normalized angular power distributions of scattered field of transmitted $|\lambda\rangle$ component and $|-\lambda\rangle$ component when the meta-device for dynamic beam-steering and polarization control capabilities evolves with $\omega_1 = -\pi/(2\mathrm{T})$ and $\omega_2 = 3\pi/(4\mathrm{T})$ for a normal LCP incidence (a, c, e). The corresponding simulation results are represented by b, d, f. The retrieved values of the deflection efficiency are indicated in a-f.

IX. Bandwidth of the meta-device in Sec. 4 of the main text

We rotated the cascaded metasurfaces with angular speeds of $\{\omega_1 = -\pi/(2\mathrm{T}), \omega_2 = \pi/(2\mathrm{T})\}$ in order to characterize the working bandwidth of the meta-device in Sec. 4 of the main text. For this, we plotted the normalized far-field scattering power distribution for the LCP incidence, with a frequency ranging from 0.5 THz to 0.9 THz and at time instants of $t=0$ and $t=0.5\mathrm{T}$, as well as plotting the absolute deflection efficiency of the transmitted LCP and RCP components (see Figs. S15 and S16). These simulated results matched very well with the theoretically calculated deflection angles $\theta = \sin^{-1}\left[2\xi_0/k_0 \cos\left[(\alpha_1(t)-\alpha_2(t))/2\right]\right]$ for the different frequencies (see Figs. S15 and S16). Following this, we further calculated the relative

14

deflection efficiency, which is defined as the ratio between the anomalously transmitted power near the deflection angle and the total transmitted power that sums up the contributions from the LCP and RCP components for the different frequencies, as shown in Fig. S17.

According to these simulated results (Figs. S15 to S17), we define the working frequency as the frequency when the corresponding absolute efficiency is larger than 25% and the relative efficiency is larger than 90%. Thus, the working bandwidth of our proposed meta-device in Sec. 4 is 0.65 THz ~ 0.75 THz.
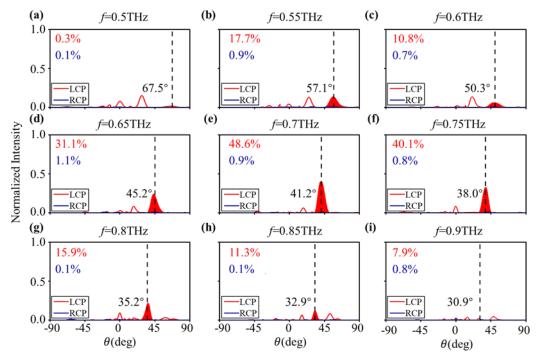

Figure S15. Simulated normalized far-field scattering power distribution of the scattered field of the transmitted LCP and RCP components when the dynamic beam-steering meta-device evolves along Path I for a normal LCP incidence with a frequency varying from 0.5 THz to 0.9 THz at the time instants t=0. The retrieved values of the absolute deflection efficiencies are indicated in a-i.
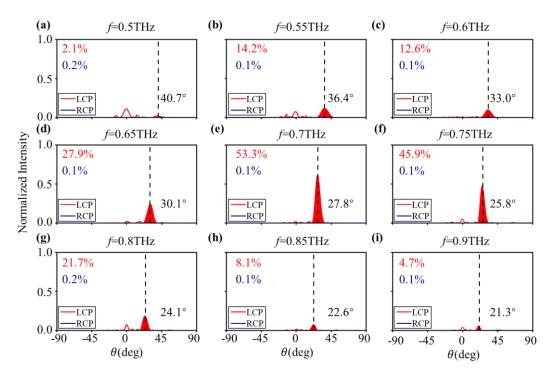
Figure S16. Simulated normalized far-field scattering power distribution of the scattered field of the transmitted LCP and RCP components when the dynamic beam-steering meta-device evolves along Path I for a normal LCP incidence with the frequency varying from 0.5 THz to 0.9 THz at the time instants t=0.5T. The retrieved values of the absolute deflection efficiencies are indicated in a-i.
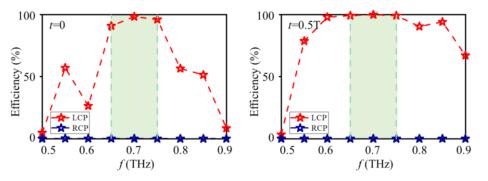

Figure S17. The relative deflection efficiency of the transmitted LCP and RCP components for the different frequencies running from 0.5 THz to 0.9 THz, with the green region denoting the working bandwidth with an absolute efficiency larger than 25% and a relative efficiency larger than 90%.

X. Angular dependence of the meta-device in Sec. 4 of the main text

Figs. S18a and b depict the theoretical and simulated normalized angular power distributions and the peak values of the transmitted components for the ideal meta-

device (assuming that they are constructed by perfectly transparent linear-gradient-phase metasurfaces). It is obvious that the peak values of the far-field distributions are monotonously decreasing as the steering angle increases, since almost all of the energy is converted to the near vicinity of the deflection angles. Here, we use the peak values of the far-field scattering power distribution to characterize our meta-device. This is because our device is demonstrated as a beam redirecting device, as opposed to as an antenna, and thus it is improper to use GAIN to characterize our meta-device. Moreover, the peak values are reduced monotonically as increasing the steering angle θ, which match very well with the relation

$$A(\theta) = A(0)\cos\theta, \tag{S7}$$

in consistency with the classical aperture angular reduction dependence. Here, $A(0)$ represents the peak value for normally transmitted wave, and $\cos\theta = \sqrt{1-\left(\xi/k_0\right)^2}$.
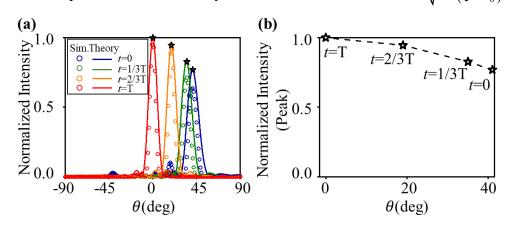

Figure S18. The theoretical and simulated far-field scattering power distributions varying with the polar angle (a), and the corresponding peak values (b).

XI. Characterization of the polarization state in Sec. 5 of the main text

This section shows how we have characterized the polarization state of the transmitted wave of the designed meta-device in Sec. 5 of the main text. Such a polarization conversion can be quantitatively analyzed through the calculated ellipticity $\cos(\Theta_f)$ and the polar angle of the polarization $\Psi_f/2$ of the transmitted wave, as shown in Fig. S19.
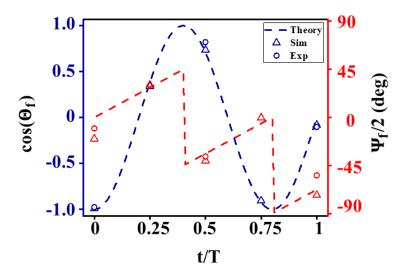
Figure S19. The calculated ellipticity $\cos(\Theta_f)$ and polar angle of the transmitted wave's polarization $\Psi_f / 2$ when the dynamic beam and polarization control meta-device evolve with $\omega_1 = -\pi / (2T)$ and $\omega_2 = 3\pi / (4T)$ for a normal LCP incidence.

On the other hand, we can also define the efficiency of polarization conversion ζ_λ as:

$$\zeta_\lambda = \frac{\left|\left(\mathbf{E}^\lambda\right)^* \cdot \mathbf{E}_\mathbf{k}^{sca}\right|^2}{\left|\left(\mathbf{E}^\lambda\right)^* \cdot \mathbf{E}_\mathbf{k}^{sca}\right|^2 + \left|\left(\mathbf{E}^{-\lambda}\right)^* \cdot \mathbf{E}_\mathbf{k}^{sca}\right|^2} \tag{S8}$$

where $\mathbf{E}^\lambda$ and $\mathbf{E}^{-\lambda}$ represent the theoretically predicted polarization of the transmitted wave and its orthogonal polarization state (calculated by Eq. (11) in the main text), and $\mathbf{E}_\mathbf{k}^{sca}$ denotes the measured (or simulated) electric field.

Fig. S20 presents the simulated and experimentally measured efficiency of the polarization conversion versus time *t*, which demonstrates a very good match with the theoretically predicted polarization, with most efficiencies surpassing 95%.
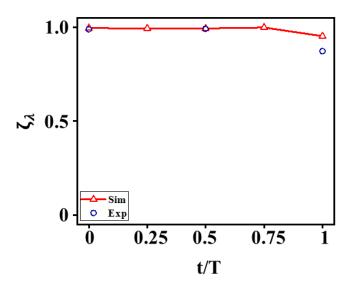
Figure S20. Simulated and experimentally measured efficiency of polarization conversion versus time t, when the dynamic beam-steering and polarization control meta-device evolves with $\omega_1 = -\pi / (2\text{T})$ and $\omega_2 = 3\pi / (4\text{T})$ for a normal LCP incidence.

XII.   Beam-forming realized by two-layer cascaded metasurface

We now design a two-layer meta-device with the phase distribution of Layer 1's metasurface being a combination of the focusing and linear gradient phases, as $\Phi_u^1(\mathbf{r}_1) = \Phi_v^1(\mathbf{r}_1) = k_0\left(\sqrt{u_1^2 + v_1^2 + f^2} - f + 0.33u_1\right)$, with $f = 500$ μm being the focal length and Layer 2 being a linear gradient phase $\Phi_u^2(\mathbf{r}_2) = \Phi_v^2(\mathbf{r}_2) = 0.33k_0u_2$, as shown in the insets of Fig. S21a. For this type of beam-steering meta-device, the incidence can no longer be limited to a plane wave but should progress to a point source or even a slot antenna. Shining the cascaded meta-device with a point source, and rotating the two layers with the angular speeds of $\{\omega_1 = -\pi / (2\text{T}), \omega_2 = \pi / (2\text{T})\}$, we plot the simulated e-field distributions at three time instants $[\, t = 0,\ (1/2)\text{T}, \text{T}\,]$ in the *xoz* plane in Fig. S21b. This indicates that the spherical wave is now converted into a plane wave with different desired directions for different time instants. The far-field distributions in Fig. S21c and the corresponding peak values in Fig. S21d also indicate that the beam-steered angles are consistent with the theoretical predications. We expect that this kind of 2D-beam-forming will have practical applications in the future.
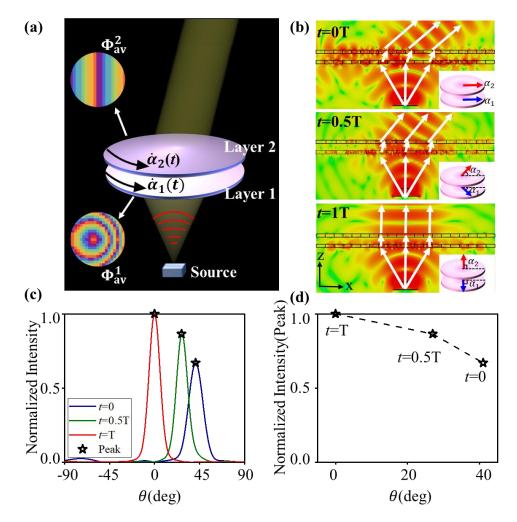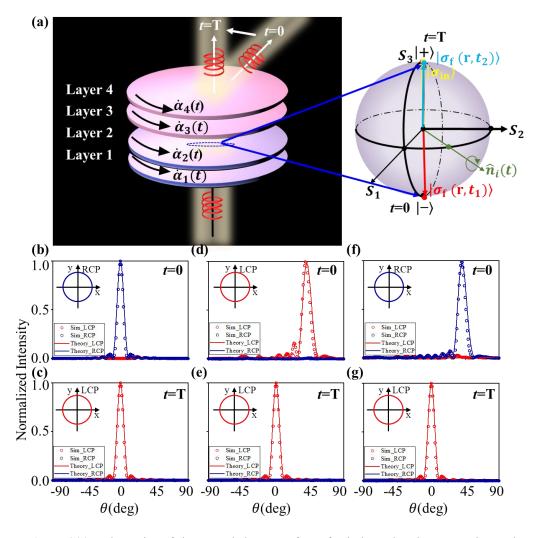
Figure S21. Schematic of the cascaded metasurfaces for the cooperative beamforming and beam-steering (a). The $|\mathbf{E}|$-field distribution in the *xoz* plane at three time instants, with the cascaded metasurface evolving with $\left\{\omega_1 = -\pi/(2T), \omega_2 = \pi/(2T)\right\}$ (b), and the corresponding far-field scattering power distribution (c) with the peak values varying with the polar angles (d).

XIII. Independent control of beam direction and polarization

Figure S22. Schematics of the cascaded metasurfaces for independent beam-steering and polarization control (a). Manipulating polarization by only rotating Layers 1 and 2 at two different time instants (b, c). Steering beam direction by only rotating Layers 3 and 4 at two different time instants (d, e). Independent control of polarization and beam direction by combining the two manipulation processes (f, g).

We now employ a four-layer cascaded metasurface as an illustration to show how to independently manipulate the wave-front and polarizations (see Fig. S22a). Here, Layers 1 and 2 are two identical anisotropic quarter-wave plates that are *only for polarization control*, and Layers 3 and 4 are two identical isotropic metasurfaces with linear-gradient phase distributions *for the purpose of beam re-directing*. Based on the similar discussion in the main text for Fig. 6a, we are able to generate any desired

polarization states on the Poincaré's sphere simply by rotating Layers 1 and 2 while keeping Layers 3 and 4 steady. For the wave-front control, we are able to rotate Layers 3 and 4 using the pre-designed angular speeds in order to realize the desired beam-steering for any incident polarizations. By combining these two wave manipulation processes together, we are able to independently control both the polarization and beam-steering angle by simply controlling the rotation angle $\{\alpha_1, \alpha_2\}$ for polarization control and $\{\alpha_3, \alpha_4\}$ wave front control. As an illustration, we now rotate Layers 1 and 2 with the angular speeds $\{\omega_1 = 0, \omega_2 = \pi/(2T)\}$ while keeping Layers 3 and 4 steady as $\{\alpha_3 = -\pi/2, \alpha_4 = \pi/2\}$. The incident LCP wave is thus converted to the normally transmitted waves with the RCP and LCP states at two time instants [t=0, T], as shown in Figs. S22b and c. We then rotate Layers 3 and 4 with the angular speeds $\{\omega_3 = -\pi/(2T), \omega_4 = \pi/(2T)\}$ while keeping Layers 1 and 2 steady as $\{\alpha_1 = 0, \alpha_2 = \pi/2\}$. After passing through Layers 1 and 2, the transmitted wave is still in an LCP state for normal LCP incidence, while the beam direction is determined by Layers 3 and 4 at two time instants [t=0, T], as shown in Figs. S22d and e. By combining these two manipulation processes together with $\{\omega_1 = 0, \omega_2 = \pi/(2T), \omega_3 = -\pi/(2T), \omega_4 = \pi/(2T)\}$, both the polarization and beam direction of the transmitted wave are able to be independently controlled, as illustrated by Figs. S22f and g.